Supplement of Ocean Sci., 21, 2041–2068, 2025
https://doi.org/10.5194/os-21-2041-2025-supplement

Ocean Science Open Access EGU

Supplement of

Physical drivers and parameter sensitivities of pearl river-derived sediment dispersal on the Northern South China Sea Shelf: a modeling study

Guang Zhang et al.

Correspondence to: Wenping Gong (gongwp@mail.sysu.edu.cn)

Introduction

This supplementary material provides additional text and figures that support the model validation and supplementary analyses of model results, which could not be fully presented in the main article. Sections S1.1 through S1.5 detail the validation process, including validation metrics and station locations (S1.1), water level validation (S1.2), wave validation (S1.3), cruise survey validation (S1.4), and mooring validation (S1.5). Section S2 presents supplementary analyses of the model results.

S1.1 Model validation metrics and station locations

The model performance was quantified using several metrics, including mean bias, root-mean-square error (RMSE), and model skill (Willmott, 1981). Bias in model validation refers to the consistent deviation between model predictions and observed data, indicating whether the model tends to overestimate or underestimate certain variables compared to actual measurements. The RMSE quantifies the average deviation between the model results and the observations. It provides a measure of the overall accuracy of the model's predictions. Model skill represents the agreement between the model and the observations. A model skill value of 1 indicates perfect agreement between the model and the observations, while a value of 0 indicates complete disagreement. The model skill is calculated as follows:

$$\mathrm{SK} = 1 - \frac{\sum_{i=1}^{N} | X_{mod} - X_{obs} |^2}{\sum_{i=1}^{N} \left(| X_{mod} - \overline{X}_{obs} | + | X_{obs} - \overline{X}_{obs} | \right)^2} \quad \text{(S1)}$$

where X_{obs} and X_{mod} are the observation and model results, respectively, $\overline{X}_{obs}$

indicates the average data, and N is the number of observations.

For model validation, field observation data from multiple stations were utilized (Figure S1), including three tidal gauge stations (Quarry Bay, Zhapo, and Qinglan), two wave measurement stations (W1 and W2), two mooring stations (M1 and M2), and 43 cruise survey stations. The validation primarily focused on key parameters such as water level, non-tide residual water level, significant wave height, current velocity, salinity, temperature, and suspended sediment concentration at these stations (Figures S2–S10). A detailed validation and analysis of these parameters are provided in the subsequent sections of this supplement.

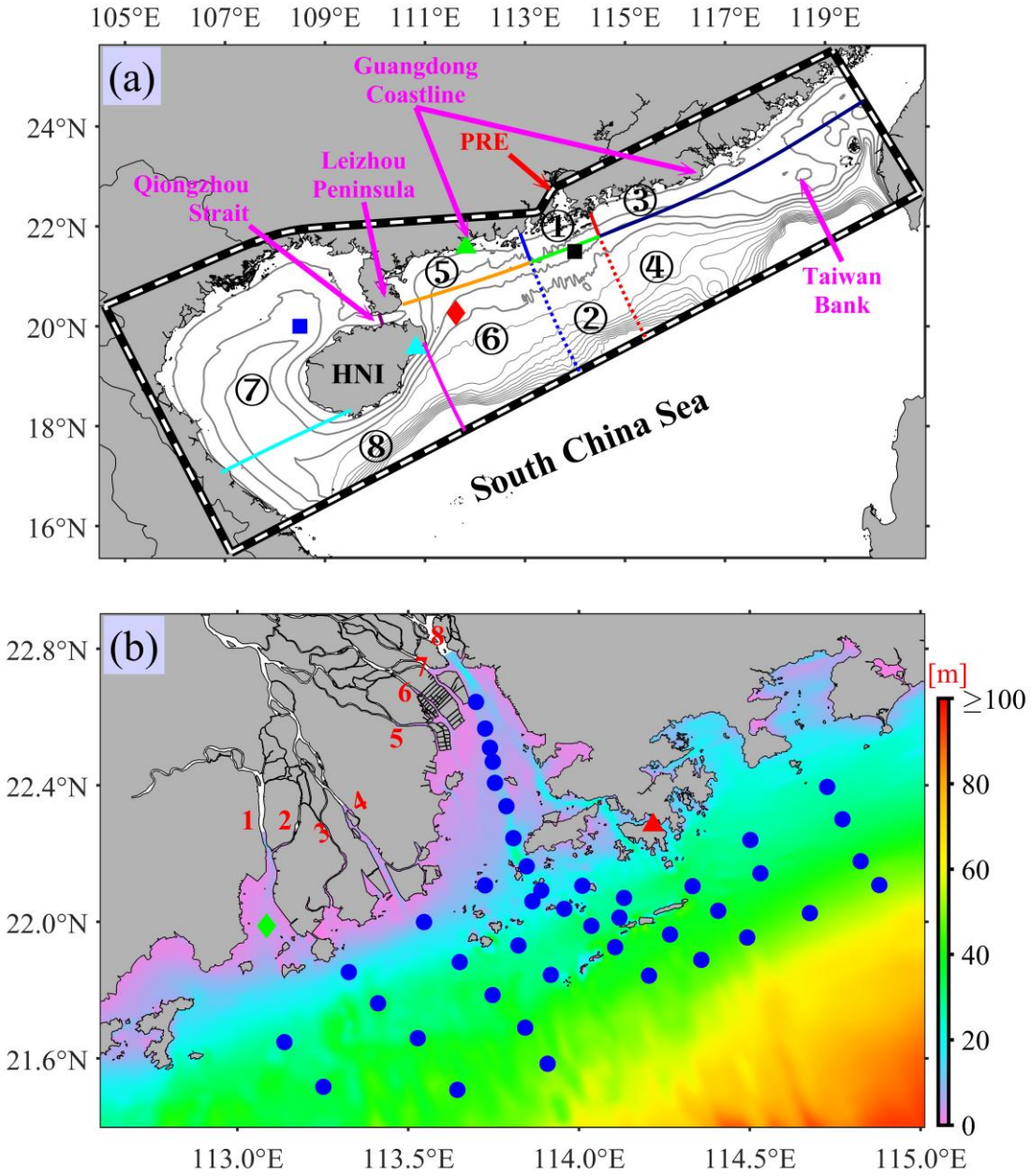

Figure S1. (a) Bathymetry contours and the model grid domain (black to white dashed lines), with circled numbers ①-⑧ indicating the eight regions: Proximal, Southern, Eastern, Southeastern, Western, Southwestern, Gulf, and Distal regions, which are delineated by transects and are described in detail in Section 4.2 of the main text. Thick gray contour lines mark the 20 to 80 m isobaths at 20 m intervals, while thin gray lines indicate the 100 to 1000 m isobaths at 100 m intervals. The abbreviations HNI and PRE refer to Hainan Island and the Pearl River Estuary, respectively. (b) A detailed bathymetry map of the PRE and nearby waters. In panel (a), observation stations are

marked by green and cyan triangles (Zhapo and Qinglan tidal gauge stations), black and blue squares (W1 and W2 wave stations), and a red diamond (M2 station), respectively. In panel (b), stations are represented by: a red triangle (Quarry Bay water level station), a green diamond (M1 station in the PRE), and blue dots (43 cruise survey stations), respectively. The red numbers 1-8 indicate the eight outlets of the PRE, where freshwater and sediment from the Pearl River (specifically the fourth and fifth sediment sizes listed in Table 1 of the main article) are discharged into the estuary.

S1.2 Water level validations

Water level observations were carried out at three tidal gauge stations: Quarry Bay, Zhapo, and Qinglan (Figures S1a-b), during distinct monitoring periods. Observations at Quarry Bay were conducted from April 1, 2017 to March 31, 2018, while those at Zhapo and Qinglan took place from January 1 to December 31, 2022. These stations were strategically located across different geographical zones relative to the Pearl River Estuary (PRE). Quarry Bay was situated in the proximal region adjacent to the PRE, while Zhapo and Qinglan were positioned in the "Western" and "Distal" regions, respectively, both located at greater distances from the PRE. Model performance was evaluated through comprehensive validation against the year-long observational records from all three stations (Figures S2-S4), comparing water level and non-tidal residual components. For water level simulations, the model achieves remarkable agreement with observations across all stations, showing RMSE below 0.26 m and skill scores surpassing 0.96. Particularly noteworthy is the model's performance in predicting non-tidal residuals, which exhibits exceptional accuracy with RMSE values

maintained under 0.11 m and skill scores consistently exceeding 0.91.

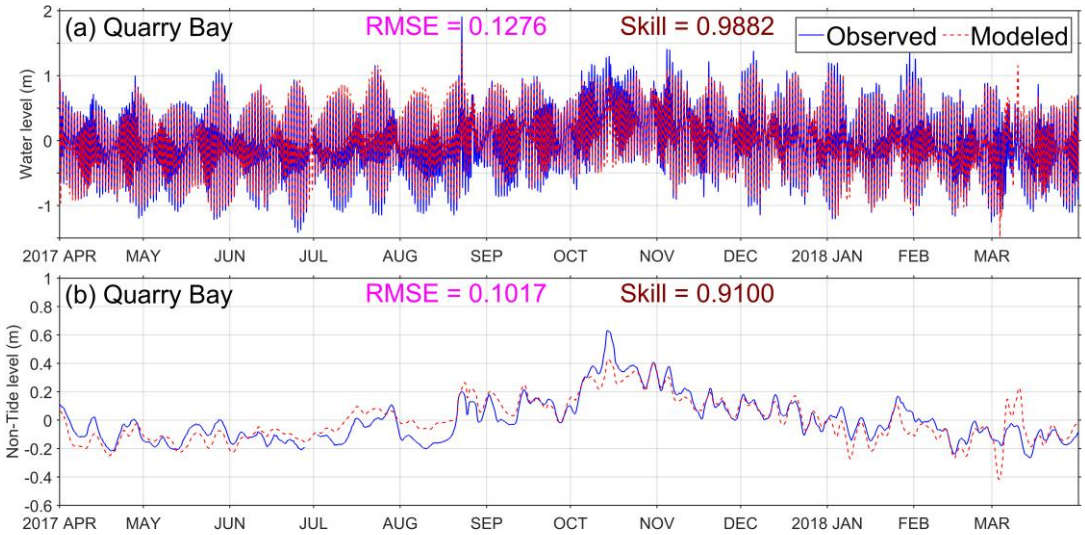

Figure S2. The validations of (a) water level and (b) non-tide level at Quarry Bay station.

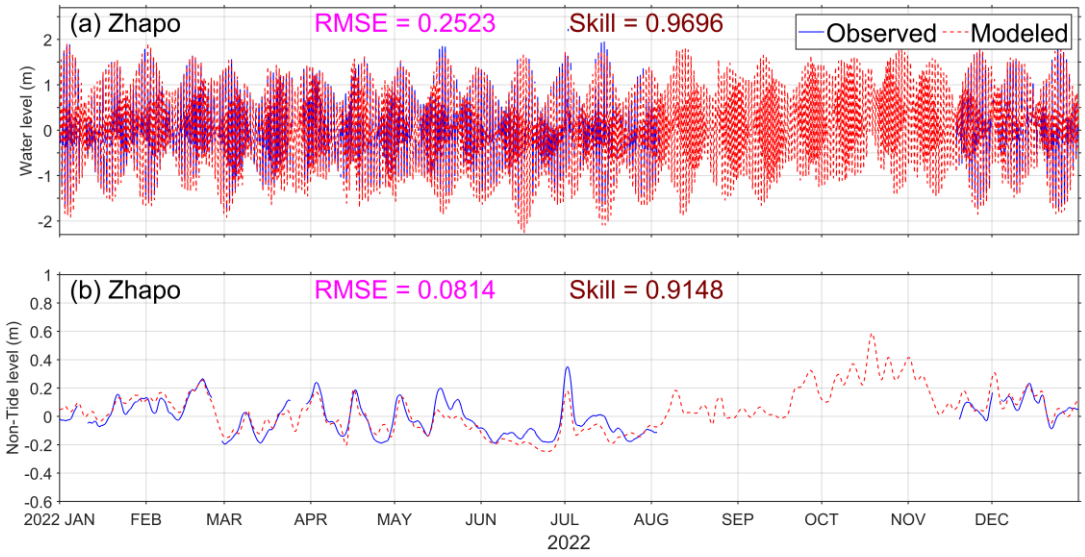

Figure S3. The validations of (a) water level and (b) non-tide level at Zhapo station.

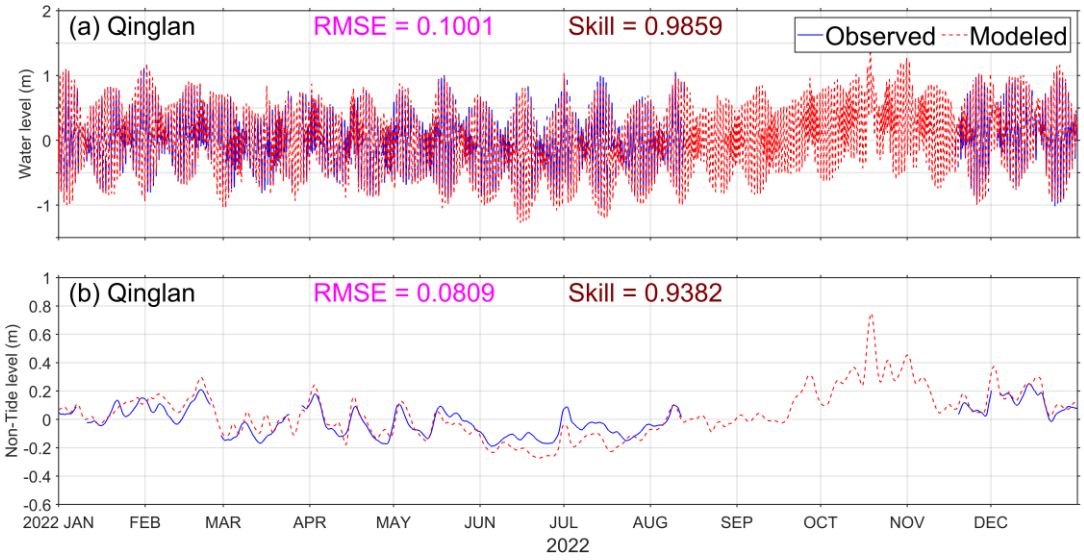

Figure S4. The validations of (a) water level and (b) non-tide level at Qinglan station.

S1.3 Wave validations

Wave data were collected at two monitoring stations (W1 and W2; Figure S1a) during two distinct periods: November 1 to December 31, 2009, and October 2 to 8, 2023, respectively. Station W1 was positioned in the "Southern" region, close to the PRE, while Station W2 was located in the Beibu Gulf, at a greater distance from the PRE (Figure S1a). The observed significant wave heights were validated against model simulations (Figures S5-S6). The model demonstrated excellent agreement with observations, achieving skill scores above 0.93 and RMSE values below 0.29 m at station W1, and skill scores exceeding 0.98 with an RMSE of 0.16 m at station W2.

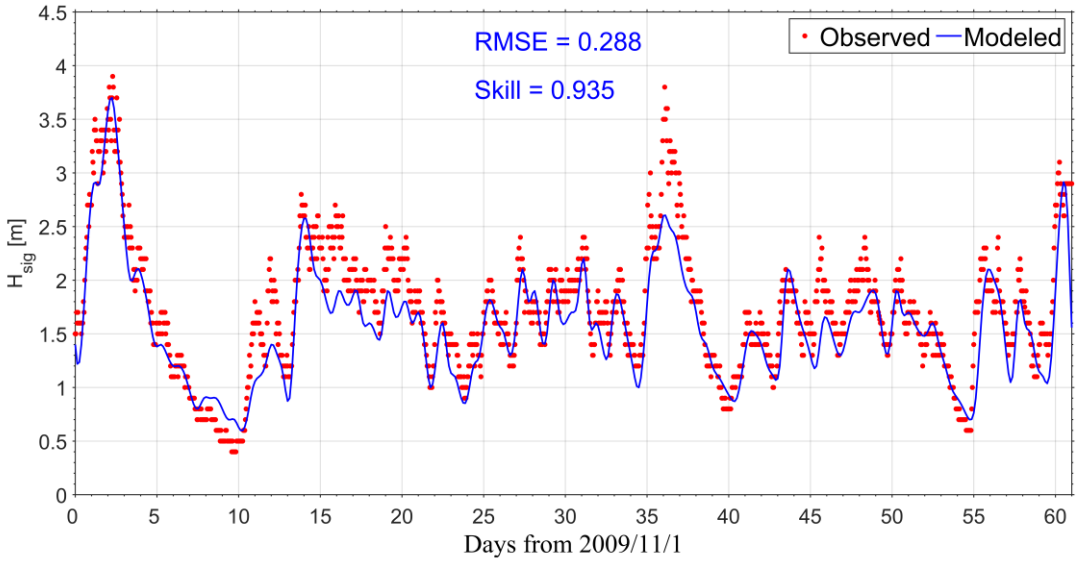

Figure S5. The validations of significant wave height at the W1 station.

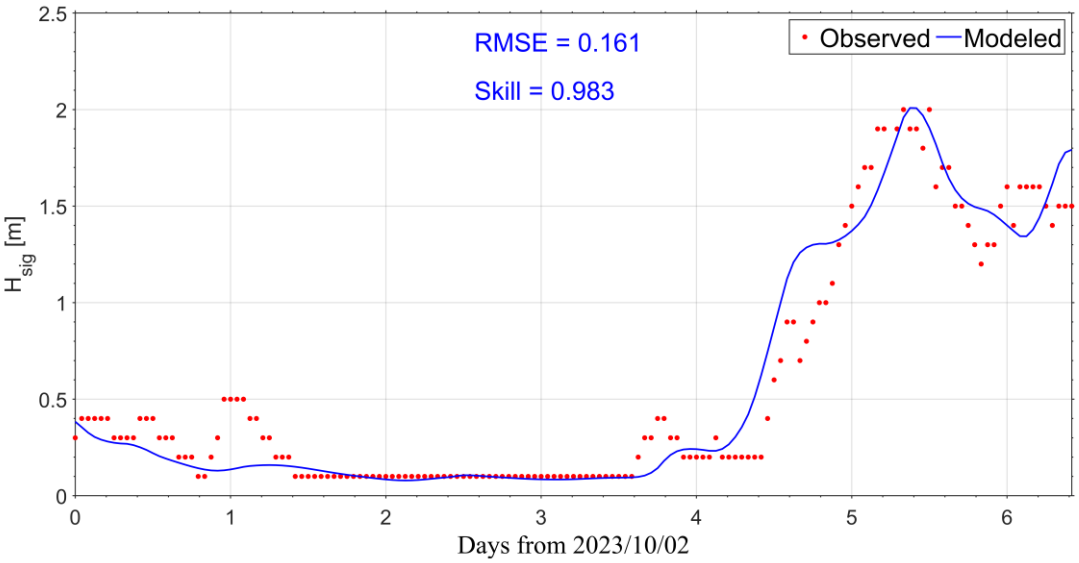

Figure S6. The validations of significant wave height at the W2 station.

S1.4 Cruise survey validations

From August 1st to 7th, 2017, Sun Yat-sen University (SYSU) conducted a cruise survey that covered the PRE and its adjacent waters on the inner shelf (Figure S1b), from onboard the R/V Changhe Ocean (Chen et al., 2019; Zhang et al., 2021b). During this period, CTD (Conductivity, Temperature, Depth) data were collected at 43 stations

(Figure S1b). These CTD measurements provided temperature and salinity profiles at various depths for each station. Additionally, surface water samples were taken and filtered to obtain SSC in the surface layer. These field data were collected to verify the accuracy of the model's predictions of salinity, temperature, and SSC. Figure S7 presents the comprehensive validation results of salinity, temperature, and SSC at 43 stations during the SYSU cruise survey.

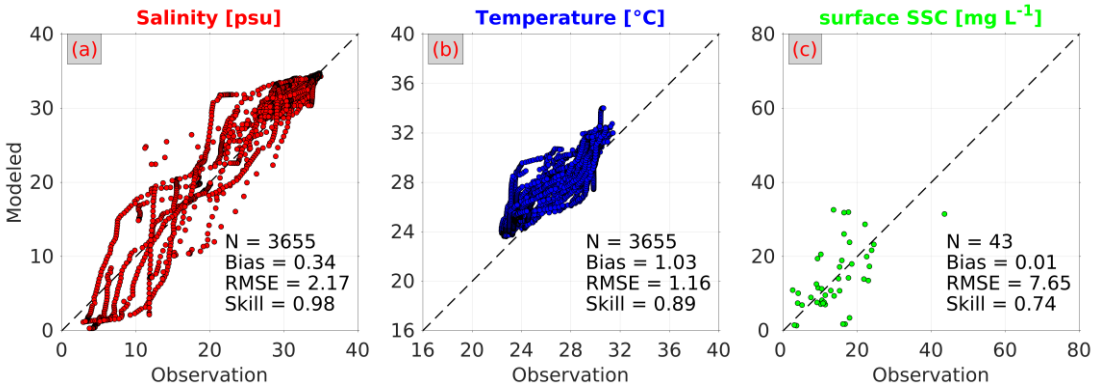

Figure S7. The validations of (a) salinity, (b) temperature, and (c) surface SSC at the 43 stations during the 2017 SYSU cruise survey.

Salinity validation exhibits excellent agreement, with a bias of merely 0.34 psu, an RMSE of 2.17 psu, and a skill value of 0.98. Temperature validation also shows relatively good performance, with both bias and RMSE at 1 degree Celsius, along with a skill value of 0.89. The validation of SSC yields reasonably good results. The small bias suggests an accurate magnitude in the model simulation. However, the RMSE of 7.65 mg L^{-1} indicates a slight deficiency in the model's capability to reproduce SSC variations over space. Nevertheless, the skill value of 0.74 indicates that the model

results remain well representative of the observed data.

S1.5 Mooring validations

From August 16 to 21, 2017, Liu et al. (2023) conducted a continuous 115-hour observation at the M1 station in the PRE (Figure S1b) and obtained data such as flow velocity, salinity, and SSC. We utilized these publicly available data to validate our model, as depicted in Figure S8.

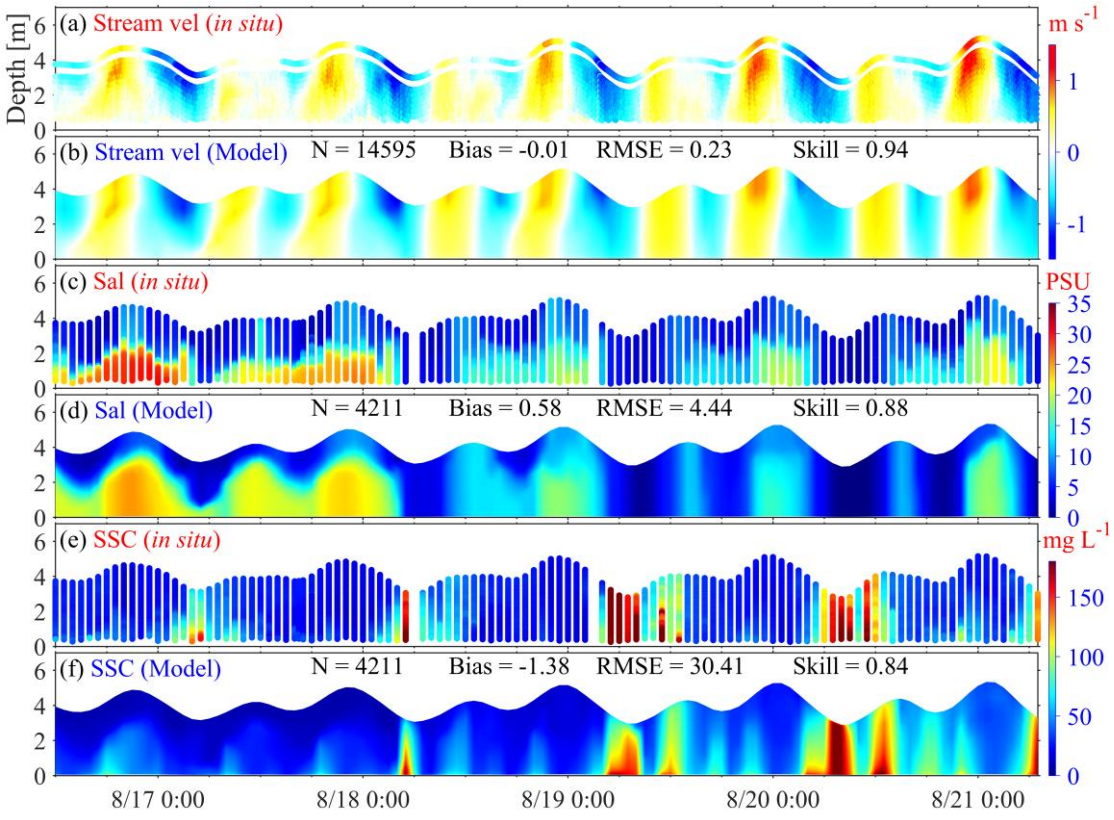

Figure S8. The validations of flow velocity, salinity, and suspended sediment concentration (SSC) of seawater at station M1, whose location is shown in Figure S1b. Rows 1, 3, and 5 display the observed data, while Rows 2, 4, and 6 showcase the corresponding model results.

The flow velocity validation demonstrates excellent agreement, with minimal bias

and RMSE, and a skill value exceeding 0.9. Salinity validation also exhibits relatively good performance, with a small bias and a skill value of 0.87. However, the RMSE exceeding 4 psu suggests that the accuracy of the seabed topography may be limited. The validation of SSC produces reasonably good results, with a small bias indicating accurate magnitude in the model simulation. Nevertheless, the RMSE of 30.4 mg L^{-1} suggests a slight deficiency in the model's ability to replicate SSC variations over time. Nonetheless, the skill value of 0.84 indicates that the model results remain well representative of the observed data.

To validate the flow velocity of our model in regions distal to the Pearl River Estuary, we employed mooring data from the M2 station as reported by Li et al. (2024). M2 station is located in the southwestern region, and its specific position, at 111.62°E and 20.27°N, can be seen in Figure S1a. The data were collected by a 300 kHz upward-looking ADCP, with a vertical resolution of 2 m and a sampling interval of 10 minutes. The data collection period spanned from January 16, 2021, to February 22, 2021. The comparison between the observations and model results is shown in Figure S9 (eastward current) and Figure S10 (northward current). It is evident that the northward current is significantly larger than the eastward current, which is influenced by the topography, and the tidal signal of the northward current is very prominent. Our model results are in good agreement with the observations, with SK values of 0.90 (Figure S9) and 0.94 (Figure S10), respectively.

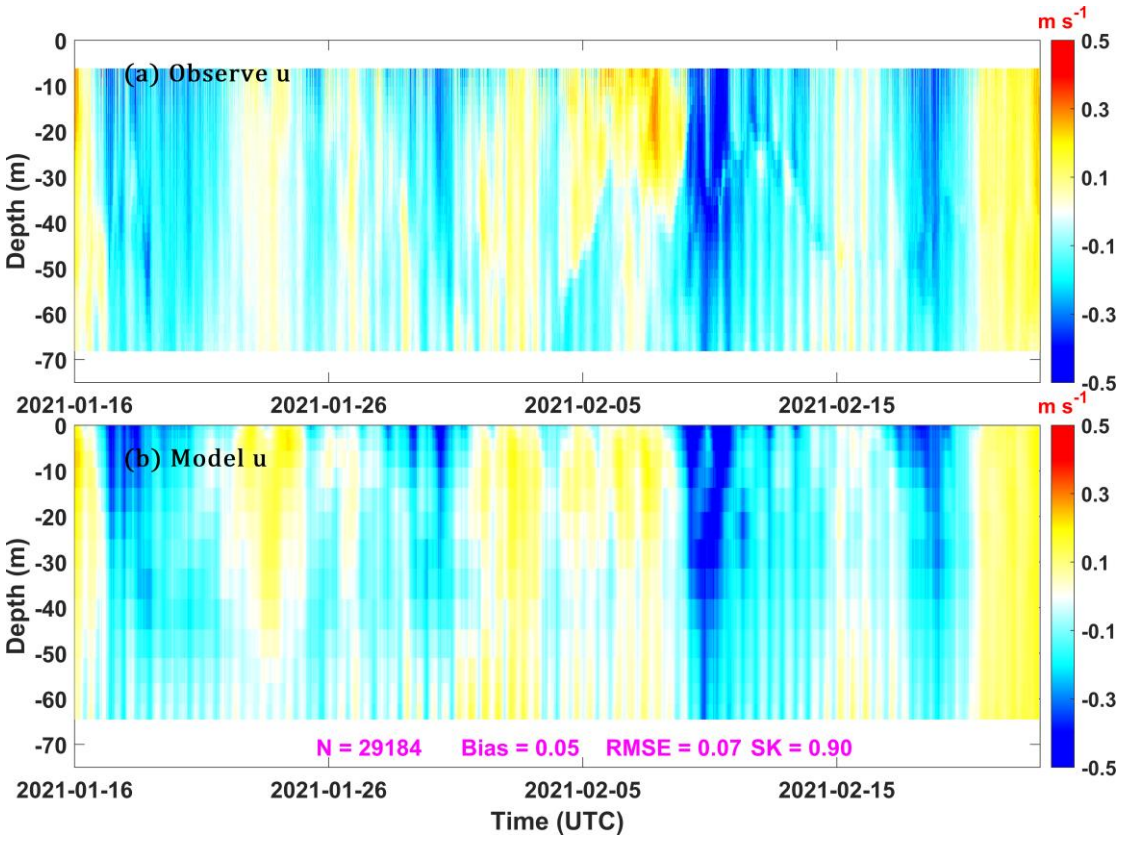

Figure S9. (a) Observed and (b) simulated eastward current velocity at M2 station.

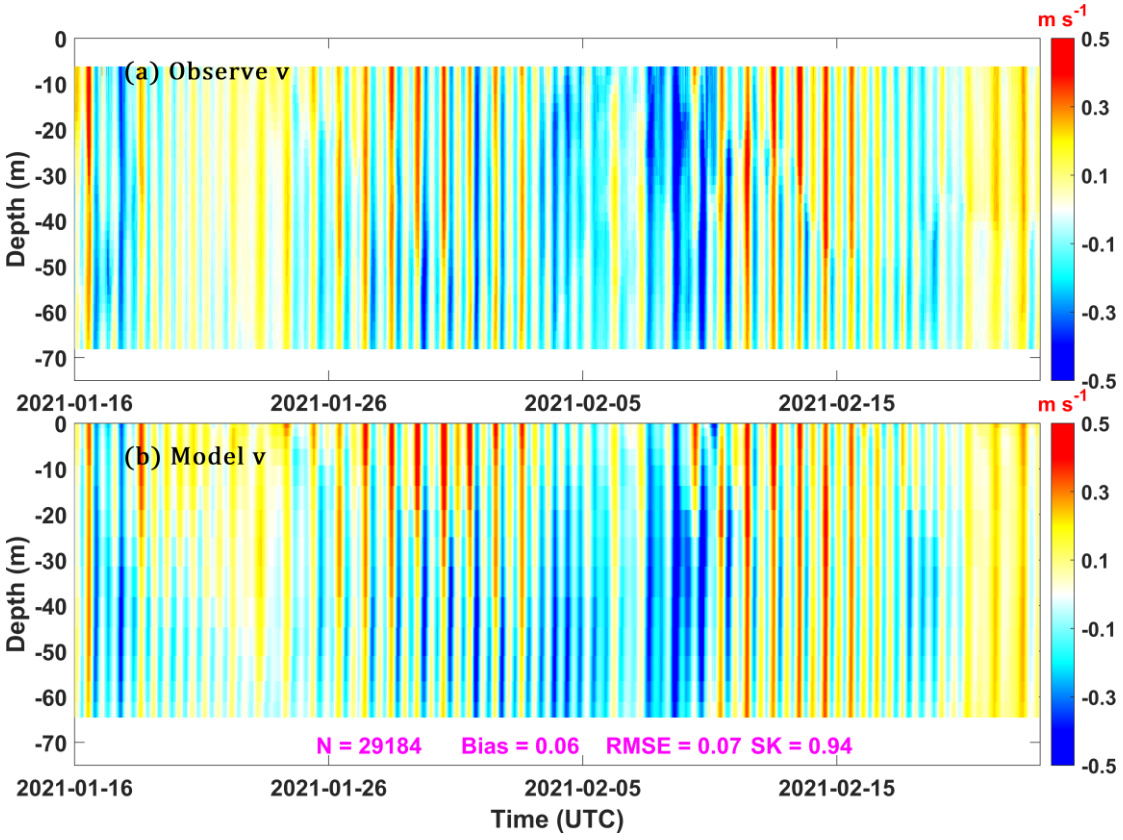

Figure S10. (a) Observed and (b) simulated northward current velocity at M2 station.

S2 Supplementary analyses of the model results

Furthermore, although the initial bed sediment grain size distribution we obtained by considering the seasonal variation of critical shear stress for erosion is quite close to the initial prototype, there are still some differences (Figures 2d-f vs. 2g-i). Additionally, the lack of in situ grain size distributions in part of the model domain (especially in the Beibu Gulf) may also introduce some uncertainties in sediment transport there. Does the spin-up duration of seabed sediments have a significant impact on the model results? It should be noted that here we are not referring to the distribution proportion of riverine sediments on the bed. To address this question, we designed a new experiment (Cycle2). We used the end state of the Control run on March 31, 2018, as the initial conditions for Cycle2. However, different from the Cycle case, in Cycle2, we changed both Class 1 and Class 4 sediments in the bed and water column at the end state of the Control run to Class 1, and both Class 2 and Class 5 sediments to Class 2. That is, there were no pre-existing Pearl River-derived sediments in the model domain when Cycle2 started. The results of Cycle2 show that the retention in the "Proximal" and "Western" regions decreased by 0.13% and 0.03% of the annual riverine sediment load, respectively, while the retention in the "Eastern", "Southeastern", "Southern", "Southwestern", "Gulf", and "Distal" regions increased by 0.03%, 0.03%, 0.01%, 0.02%, 0.07%, and 0.01%, respectively. This suggests that uncertainty in seabed sediment spin-up duration has a relatively minor impact.

We employ the COAWST model, which uses an S-coordinate system in the vertical direction with increased resolution near the surface and bottom layers (Song and

174 Haidvogel, 1994). This vertical layering allows cell heights to vary, enabling finer
175 resolution in dynamically important regions and improving performance in areas with
176 sloping bathymetry compared to traditional sigma-coordinate systems (Bryan, 1969;
177 Song and Haidvogel, 1994). In addition, our model includes horizontal grid refinement
178 in the PRE, enhancing its ability to resolve estuarine features.

179 Our model effectively captures estuarine turbidity maxima (ETM) and horizontal
180 salinity fronts (Figures S11 and S12). During summer, multiple ETMs appear near the
181 estuary bottom (Figure S11b), and while these features persist in winter, their
182 concentrations vary (Figure S12b), consistent with the findings of Wang et al. (2018),
183 Zhan et al. (2019), Zhang et al. (2021a), Ma et al. (2022), and Ma et al. (2024).
184 Horizontal salinity fronts (Regions where the horizontal salinity gradient magnitude
185 (SGM) exceeds 1.5 psu km^{-1}) are also well represented, showing an upstream shift from
186 the high-discharge summer season to the low-discharge winter season (Figures S11e–f
187 and S12e–f), in agreement with previous studies by Zhang et al. (2021a)_ENREF_138
188 and Ma et al. (2024).

189 The fronts in estuaries always exhibit high convergence of currents in their vicinity
190 (Geyer and Ralston, 2015), and thus exert a great influence on sediment transport and
191 trapping (Ralston et al., 2012). One important trapping mechanism is the near-bottom
192 velocity convergence caused by the longitudinal or lateral gradients in the baroclinic
193 pressure gradient, which creates regions of estuarine turbidity maxima and high
194 deposition (Meade, 1969; Burchard and Baumert, 1998; Burchard et al., 2018). The
195 surface frontal zone always exhibits flow convergence with significant downwelling or

196 sinking flow (Garvine and Monk, 1974; O'Donnell et al., 1998; Marmorino and Trump,
197 2000), which favors sediment settling and deposition there.

198 Within the PRE, pronounced horizontal salinity gradients exist between channels
199 and shoals, as well as between the estuary and the shelf (Figures S11e–f and S12e–f).
200 These gradients facilitate significant trapping of Pearl River–derived sediment near the
201 estuary, particularly on the estuarine shoals and at the river mouth (Zhang et al., 2019).
202 During winter, the Pearl River's freshwater discharge is low and comes mainly from
203 the western outlets (Wong et al., 2003b). Furthermore, the Coriolis force and the
204 downwelling-favorable wind steer freshwater toward the western shore (Wong et al.,
205 2003b; Lai et al., 2016). The convergence between the seaward diluted water and the
206 saline coastal water establishes a strong salinity front along the western shore, where
207 the strongest seaward flow exists (Wong et al., 2003a). In winter, the upstream and
208 northwestward migration of salinity fronts enhances the lateral trapping of sediment on
209 the West shoal of the Pearl River Estuary (Zhang et al., 2021a).

210

211

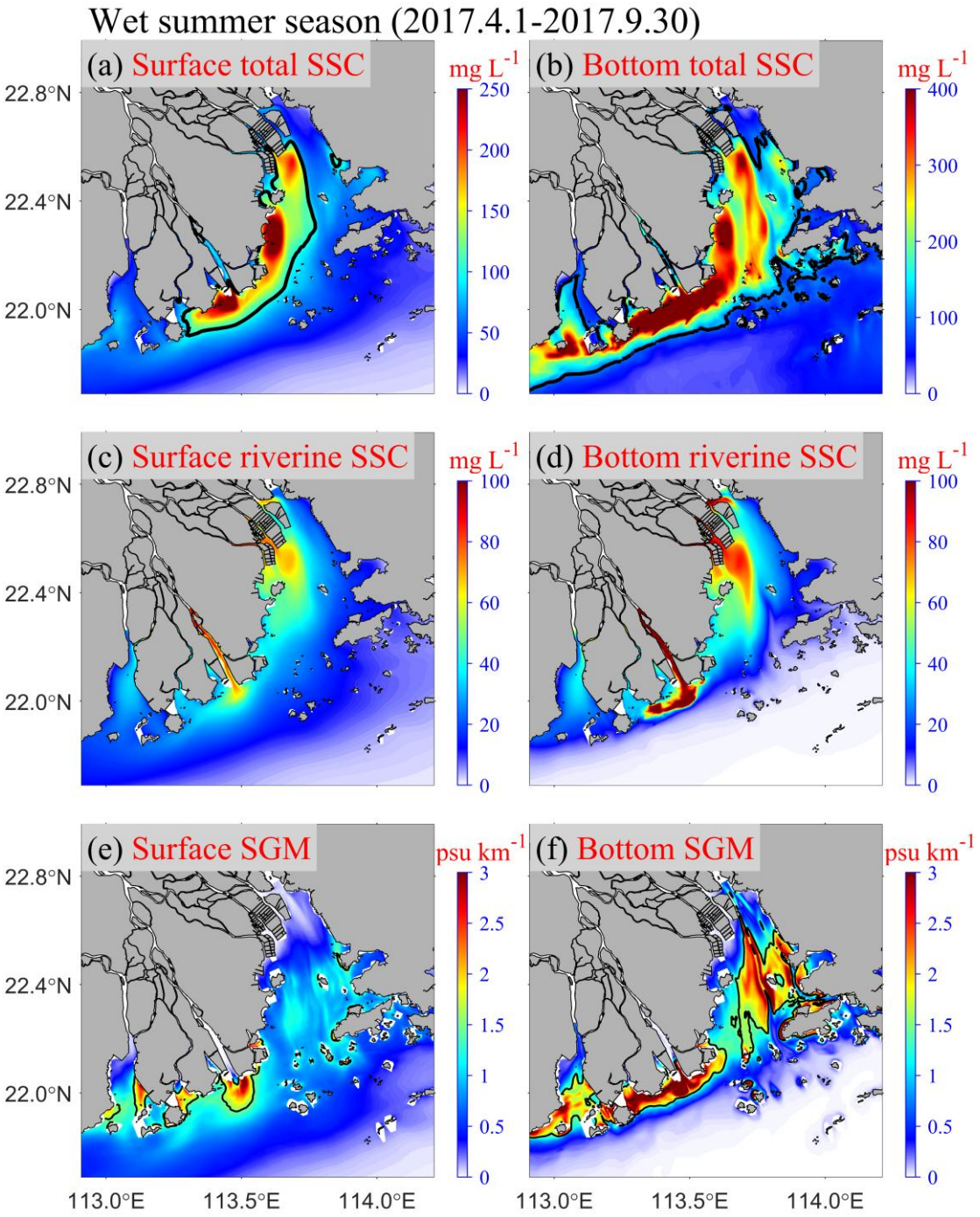

212

213 **Figure S11.** Summer-averaged (a–b) total suspended sediment concentration (classes

214 1–5 in Table 1) and the black lines mark the 100 mg L^{-1} contours, (c–d) Pearl River–

215 derived suspended sediment concentration (classes 4–5 in Table 1), and (e–f) horizontal

216 salinity gradient magnitude (SGM) and the black lines mark the 1.5 psu km^{-1} contours.

217 Columns 1 and 2 represent surface and bottom layers, respectively.

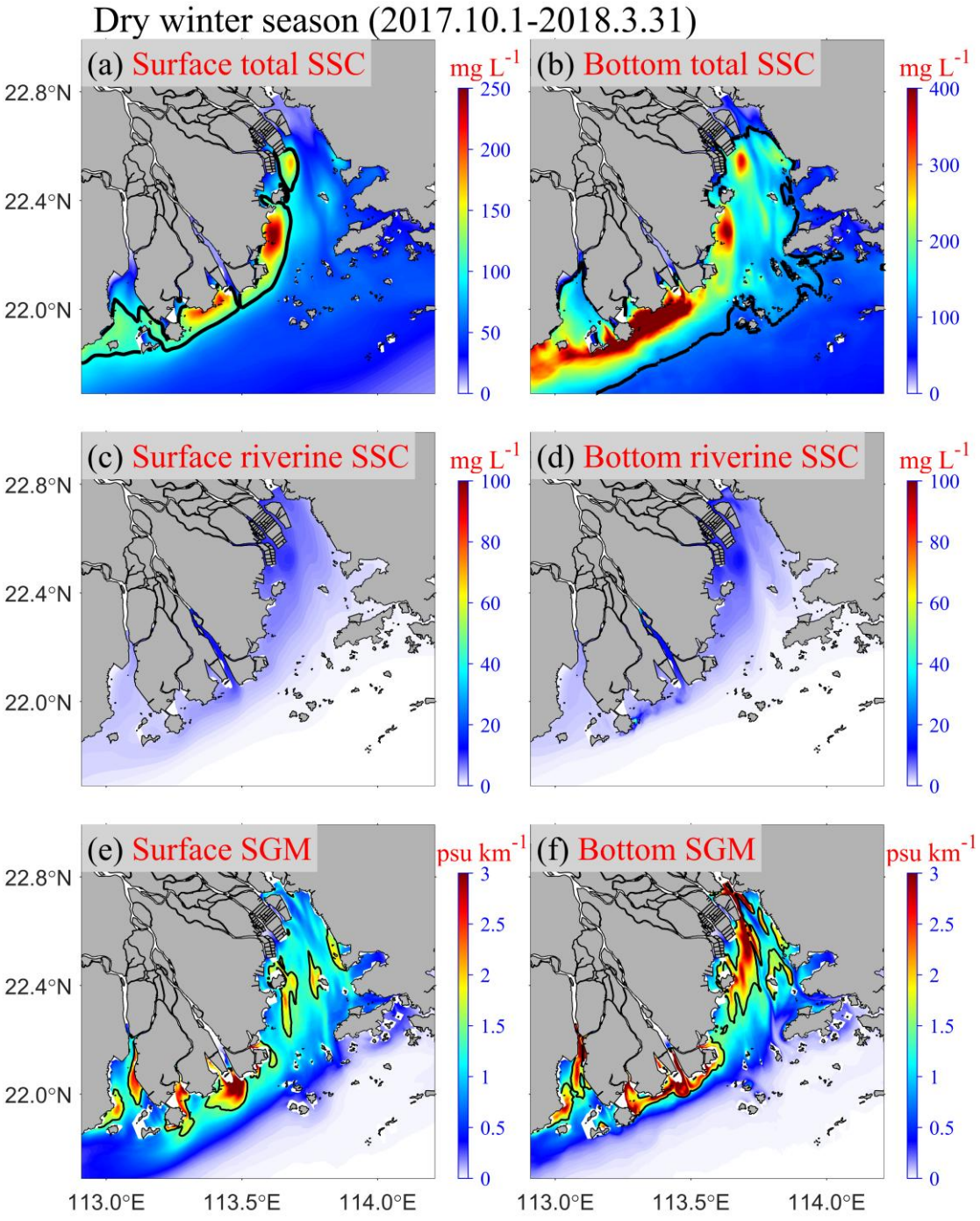

Figure S12. Same as Figure S11, but for winter-averaged ones.

References

Bryan, K., 1969. A numerical method for the study of the circulation of the world ocean. Journal of Computational Physics 4, 347-376.

Burchard, H., Baumert, H., 1998. The Formation of Estuarine Turbidity Maxima Due to Density Effects in the Salt Wedge. A Hydrodynamic Process Study. Journal of Physical Oceanography 28, 309-321.

Burchard, H., Schuttelaars, H.M., Ralston, D.K., 2018. Sediment Trapping in Estuaries. Annual Review of Marine Science 10, 371-395.

Chen, Y., Chen, L., Zhang, H., Gong, W., 2019. Effects of wave-current interaction on the Pearl River Estuary during Typhoon Hato. Estuarine, Coastal and Shelf Science 228, 106364.

Garvine, R.W., Monk, J.D., 1974. Frontal structure of a river plume. Journal of Geophysical Research 79, 2251-2259.

Geyer, W.R., Ralston, D.K., 2015. Estuarine Frontogenesis. Journal of Physical Oceanography 45, 546-561.

Lai, Z., Ma, R., Huang, M., Chen, C., Chen, Y., Xie, C., Beardsley, R.C., 2016. Downwelling wind, tides, and estuarine plume dynamics. Journal of Geophysical Research: Oceans 121, 4245-4263.

Li, J., Li, M., Xie, L., 2024. Observations of near-inertial oscillations trapped at inclined front on continental shelf of the northwestern South China Sea. EGUsphere 2024, 1-25.

Liu, H., Ye, L., Zhou, W., Wu, J., 2023. Salt-wedge intrusion-retreat cycle induced sediment floc dynamics in bottom boundary layer (BBL) of a micro-tidal estuary. Marine Geology 466, 107175.

Ma, C., Zhao, J., Ai, B., Sun, S., Yang, Z., 2022. Machine Learning Based Long - Term Water Quality in the Turbid Pearl River Estuary, China. Journal of Geophysical Research: Oceans 127.

Ma, M., Porz, L., Schrum, C., Zhang, W., 2024. Physical mechanisms, dynamics and interconnections of multiple estuarine turbidity maximum in the Pearl River estuary. Frontiers in Marine Science Volume 11 - 2024.

Marmorino, G.O., Trump, C.L., 2000. Gravity current structure of the Chesapeake Bay outflow plume. Journal of Geophysical Research: Oceans 105, 28847-28861.

Meade, R.H., 1969. Landward Transport of Bottom Sediments in Estuaries of the Atlantic Coastal Plain. Journal of Sedimentary Petrology 39, 222-234.

O'Donnell, J., Marmorino, G.O., Trump, C.L., 1998. Convergence and Downwelling at a River Plume

Front. Journal of Physical Oceanography 28, 1481-1495.

Ralston, D.K., Geyer, W.R., Warner, J.C., 2012. Bathymetric controls on sediment transport in the Hudson River estuary: Lateral asymmetry and frontal trapping. Journal of Geophysical Research: Oceans 117.

Song, Y., Haidvogel, D., 1994. A Semi-implicit Ocean Circulation Model Using a Generalized Topography-Following Coordinate System. Journal of Computational Physics 115, 228-244.

Wang, C., Li, W., Chen, S., Li, D., Wang, D., Liu, J., 2018. The spatial and temporal variation of total suspended solid concentration in Pearl River Estuary during 1987-2015 based on remote sensing. Science of The Total Environment 618, 1125-1138.

Willmott, C.J., 1981. On the Validation Of Models. Physical Geography 2, 184-194.

Wong, L.A., Chen, J.C., Xue, H., Dong, L.X., Guan, W.B., Su, J.L., 2003a. A model study of the circulation in the Pearl River Estuary (PRE) and its adjacent coastal waters: 2. Sensitivity experiments. Journal of Geophysical Research 108.

Wong, L.A., Chen, J.C., Xue, H., Dong, L.X., Su, J.L., Heinke, G., 2003b. A model study of the circulation in the Pearl River Estuary (PRE) and its adjacent coastal waters: 1. Simulations and comparison with observations. Journal of Geophysical Research 108.

Zhan, W., Wu, J., Wei, X., Tang, S., Zhan, H., 2019. Spatio-temporal variation of the suspended sediment concentration in the Pearl River Estuary observed by MODIS during 2003–2015. Continental Shelf Research 172, 22-32.

Zhang, G., Chen, Y., Cheng, W., Zhang, H., Gong, W., 2021a. Wave Effects on Sediment Transport and Entrapment in a Channel-Shoal Estuary: The Pearl River Estuary in the Dry Winter Season. Journal of Geophysical Research: Oceans 126.

Zhang, G., Cheng, W., Chen, L., Zhang, H., Gong, W., 2019. Transport of riverine sediment from different outlets in the Pearl River Estuary during the wet season. Marine Geology 415, 105957.

Zhang, H., Hu, S., Cheng, W., Zhu, L., Chen, Y., Liu, J., Gong, W., Li, Y., Li, S., 2021b. Response of freshwater transport during typhoons with wave-induced mixing effects in the Pearl River Estuary, China. Estuarine, Coastal and Shelf Science 258, 107439.